Functional Susceptibility Weighted Magnetic Resonance Imaging

Markus Barth and Daniel B. Rowe

Version 7/14/2009

ABSTRACT

In this chapter we describe the basics of BOLD based fMRI starting from the point already described in previous chapters (the paramagnetism of deoxyhaemolobin and its consequences for the MR signal). This will include the current view on the influence of physiological parameters (CBF, CBV and $CMRO_2$) on the BOLD signal, the link to neuronal activation and its temporal profile. Furthermore, this chapter describes relevant vascular and anatomical features of the brain with an emphasis on the venous side and how these anatomical and physiological properties influence the MR signal. We describe how a fast, high resolution SWI sequence can be used to perform BOLD-based fMRI (= functional SWI) in order to learn more about the contributions of different tissue compartments (gray matter, veins) to the fMRI signal. As the SWI sequence is able to resolve small venous structures the magnitude and phase behavior of veins can be visualized, quantified and veins can be removed from the functional data based on this information. We then describe the phase changes in the (f)MR signal from magnetic field changes in and around vessels quantitatively and use it to detect veins in a standard (i.e. lower spatial resolution) fMRI setup. This is being used in the statistical modeling of complex-valued voxel fMRI measurements in terms of magnitude and phase along with detection of statistically significant changes. We present the results of applying the complex constant phase model to reduce fMRI activation in voxels that have task related phase changes.

Key words: fMRI, SWI, Phase Imaging, Susceptibility Weighted Imaging

STRUCTURE:

Introduction

Functional Magnetic Resonance Imaging (fMRI) based on the blood oxygenation level dependent (BOLD) effect has found widespread applications in neuroscience and medicine since its detection in the early 1990's [1,2] by using it to map regions of the brain that are 'activated' during performance of a specific task. The form of contrast that is used in fMRI is provided by dynamically measuring the blood oxygenation level dependent (BOLD) contrast, using image time series to assess the haemodynamic response related to neural activity in the brain [3]. This is possible because changes in blood flow and blood oxygenation in the brain (collectively known as haemodynamics) are linked to neural activity. When nerve cells are active more oxygen is needed locally which is extracted from hemoglobin containing red blood cells in local capillaries. Importantly, this local increase in oxygen consumption leads to an increase in blood flow, delayed by approximately 1-2 seconds. This haemodynamic response reaches a peak after 4-5 seconds, before falling back to baseline (and typically undershooting). Consequently, the relative concentrations of oxyhaemoglobin [HbO] and deoxyhaemoglobin ([dHb]) change locally, as well as the regional blood flow (CBF) and blood volume (CBV). The BOLD signal change amounts to (see e.g. [4])

$$\frac{\Delta BOLD}{BOLD} = M \cdot \left(1 - \left(\frac{CMR_{O_2}}{CMR_{O_2}\mid_0}\right)^{\beta} \cdot \left(\frac{CBF}{CBF_0}\right)^{\alpha-\beta}\right) \qquad [1]$$

where

$$M \equiv TE \cdot A \cdot CBV_0 \cdot [dHB]_{v_0}^{\beta} \qquad [2]$$

and

$$\frac{\Delta CBV}{CBV} = \left(\frac{CBF}{CBF_0}\right)^{\alpha}$$

[3]

where α is a constant that relates *CBF* changes to *CBV* changes. The parameter α has been determined experimentally to 0.38 [5] and 0.5 [6]. The parameter *A* is a field strength and sample-specific proportionality constant and β is a constant, in the range $1 < \beta < 2$ that depends on the average blood volume within a tissue sample.

Because haemoglobin is diamagnetic when oxygenated but paramagnetic when deoxygenated, the interplay of these haemodynamic processes results in a net change in the magnetic susceptibility of blood, which in turn leads to a slight change in the local magnetic field and hence in the MR signal intensity. The MRI signal of blood is therefore dependent on the level of oxygenation which can be detected using an appropriate MR pulse sequence. The BOLD effect is commonly measured using the rapid acquisition of a series of two-dimensional images with a contrast heavily weighted by the local inhomogeneities of the magnetic field as caused by deoxyhaemoglobin. This technique is called gradient echo, echo planar imaging (EPI). Such images can be acquired with moderately good spatial and temporal resolution; the whole-brain is usually covered with a spatial resolution of about 3 millimeters and a temporal resolution of about 2–3 seconds. Recent technical advancements, such as the use of high magnetic fields and advanced "multichannel" RF reception, have advanced spatial resolution to the millimeter scale. Although the haemodynamic response takes several seconds, BOLD responses to stimuli presented as close together as one or two seconds can be distinguished from one another, using a method known as event-related fMRI. Using differently designed MR pulse sequences, changes in cerebral blood flow (CBF) or blood volume (CBV) can also be measured directly.

The influence of venous structures on the spatial localization and functional specificity in BOLD fMRI

The BOLD signal is mainly composed of signal contributions from larger veins, smaller venules, and capillaries, i.e. where dHb concentration changes significantly. It has been shown that larger venous vessels give rise to a significant portion of the observed BOLD activation both in gradient-echo fMRI [7-13] but also using spin-echo fMRI [14]. This leads to spurious activations and an intrinsic degradation of the spatial localization and reduced functional specificity as significant activation may be found far from the site of neuronal activation. Using BOLD fMRI this cannot be achieved by simply increasing nominal spatial resolution. However, experimental results indicate that the BOLD signal can be weighted towards the smaller vessels, and hence closer to the active neurons, by using larger magnetic fields. It has been estimated that about 70% of the BOLD signal arises from larger vessels in a 1.5 Tesla scanner, but about 70% arises from smaller vessels at 7 Tesla. Furthermore, the size of the BOLD signal originating from the capillaries increases roughly as the square of the magnetic field strength and hence there has been a push for higher field scanners to improve both localization and sensitivity.

As the venous part of the vasculature is relevant for BOLD fMRI, knowledge about venous vasculature is very important. From an anatomical point of view venous vessels in the brain can be classified into several categories [15]: The large cortical cerebral veins that drain the hemispheres; the (extracortical) pial venous network that drains the lobules; and the intracortical vascular network. The diameters of venous vessels span a vast range from the very small venules (10 μm diameter) to the large sagittal sinus (diameter >10 mm; see Table 1 for a summary of

some vessel properties [16]). The venules – that run approximately parallel to the cortical surface – are part of the intracortical vascular network where they drain the capillary bed. The venules in turn are connected to intracortical veins that can be divided into several groups depending on which cortical layer they drain ([15], Fig. 1). Importantly for fMRI these intracortical veins (diameter ~ 80 μm) emerge from the cortex roughly at a right angle and connect to the pial vein network (vein diameter > 200 μm). Summarizing the flow of the blood in the venous side, this means that venous blood is first drained within a layer to an intracortical vein that connects the vascular layers and leads to the cortical surface (Fig. 1a). The venous blood then draines along the cortical surface leading away from the respective cortical area (Fig. 1b). From this anatomical argument it becomes clear that functional signal changes detected in large (thus: extracortical) veins can severely compromise functional localization and specificity. Duvernoy et al. [15] also define a vertical vascular unit centered around a large intracortical vein (also called principal intracortical vein) and is surrounded by a ring of arteries which gives it a column-like appearance.

[Figure 1 about here]
[Table 1 about here]

From the seminal papers of Ogawa which triggered the use of the BOLD effect in fMRI [1,2], but also from previous chapters we know that a large venous vessel leads to a large signal reduction in its respective MR signal in a T2*-weighted sequence. From the very beginning of

fMRI it was thus thought that also a certain amount of the functional signal *change* (thus: "activation") could originate from large venous vessels. The problem is that the larger the vein the further away it presumably is from the functional area where the neuronal activation occurs. The estimations for the distance where "functional activation" can still be detected range from 4.2 mm [17] to three times that amount [18] using the Turner model updated with recently found vascular properties of human gray matter microcirculation. Boxerman et al. [19] showed by using Monte-Carlo simulations with a cylindrical vein model that a spin echo sequence is primarily susceptible to capillaries whereas a gradient echo sequence is most sensitive to veins larger than capillaries (diameter > 10 μm, see Fig. 2). However, because of the big influence of vascular geometry and geometric parameters (vessel size, distribution of veins within a voxel, orientation of the vessel to B_0) on the venous signal in a gradient echo sequence it is still difficult to estimate the exact amount of extracortical vein contribution. One could argue that spin echo sequences should be used in fMRI because they are more susceptible to the capillary bed, but this increase in specificity comes at a largely reduced sensitivity (about a factor of 3) which is normally not an option for a standard fMRI experiment.

[Figure 2 about here]

Functional SWI (fSWI)

To get a clearer view on the influence of veins on the BOLD fMRI signal, the SWI technique can be used to directly depict the venous vasculature in a functional experiment. Due to significant improvements in scanner hardware (high field scanners, coil arrays) and imaging methods (e.g. parallel imaging) it is now possible to achieve very high isotropic resolution in functional MRI

where veins can be identified directly and the contribution can then be estimated based on their spatial location rather than on guesses based on model calculations. As described in previous chapters the identification is due to the BOLD effect itself when using very high-resolution 3D gradient echo data sets, even down to a diameter of 100-200 μm in humans, depending on field strength [20-22]. However, a very high spatial resolution is normally detrimental to performing fMRI and is not (easily) achieved with commonly used multi-slice 2D EPI. At first, it would further increase the geometric distortions that also make a direct mapping of EPI data sets onto non-EPI anatomical or – in this case – venographic data sets problematic. Secondly, the contrast of veins in high resolution EPI is lower than in corresponding SWI data sets, most probably due to T_2^* blurring related to the long EPI readout. Nevertheless, some studies attempted to identify veins [20-22] based on a rather course resolution at least in the slice direction (typically 3-5 mm). This leads to partial volume effects significantly limiting identification of small veins. However, once the functional (magnitude and phase) characteristics are established in high resolution studies, one can go back to lower resolution and try to use this information to reduce the influence of veins in a standard fMRI experiment. So attempts can be made to account for large vein effects by making use of their functional properties, e.g. setting a threshold for the functional signal change, see e.g. [26], using their phase behaviour [27-30]. Other studies reduced their influence by using diffusion weighting to at least remove their intravascular effects at different field strengths [31-33].

The SWI sequence as described in Imaging Protocol 1 of Appendix B was used in an fMRI experiment that was confined to the visual cortex and accelerated sufficiently to be compatible with a block design. See Fig. 3a for localization of the 3D slab and Fig. 3b for one sample image

from the functional data set. One can clearly see that the image in Fig. 3b lacks the geometrical distortion that is common in EPI. It is also possible to identify venous vessels directly in this functional image.

[Figure 3 about here]

When performing a visual task, the activation pattern (the statistical map) computed using the methods described in Appendix A clearly shows tubular structures that can be identified as veins by comparison with the venous vascular tree that is segmented from the functional data itself (see Fig. 4a). Due to the negligible geometrical distortion it is straightforward to overlay the significant activation – after removing the venous effects – on the corresponding anatomical slices (Fig. 4b). The contribution of veins visible in the functional data to the activation volume was found to be one quarter. The signal change maps (fig. 4c, 2 subjects) show the venous structures even more clearly. Importantly, the venous vasculature differs significantly from subject to subject which shows how the individual vascularization might impact on the functional localization and its variability. Many studies have examined the reproducibility of functional activation and one of the largest variation was found between subjects. Besides other factors, the variability of the venous vascular network might well be an important factor of inter-individual variability as is also suggested by a study by Cusack et al.[34].

[Figure 4 about here]

When analyzing the functional (per cent) signal changes of a vein compared to cortical region (Fig. 5a), it clearly shows the huge signal changes that occur in veins at this high spatial resolution, and also how the signal change comes closer to that of cortical regions in which the signal change is essentially independent of resolution. At a commonly used spatial resolution of about 4 mm voxel size, cortical activation and signal changes in veins cannot be separated easily any more. However, at this very high resolution used here a signal change threshold (% signal change in the cortical region + one standard deviation) can clearly eliminate the majority of vein effects (Fig. 5b). The results of this study also enable a rough estimation of how long "activation" can maximally travel along the draining veins by just counting the voxels of the long tubular structures. The result of 40-50 mm is a factor 10 larger than expected from the original estimation of Turner [17] and still a factor of 3 larger than the one from Lauwers et al. [18]. One factor explaining the discrepancy is that in the model an activated surface of only 1 cm^3 is assumed, while the visual task used in the fSWI certainly activates a larger area. When performing a similar experiment at 7 Tesla (Fig. 5c) one can see that the influence of veins – i.e. the appearance of tubular structures in the activation map – is clearly reduced.

[Figure 5 about here]

Susceptibility Induced Phase Changes

Another confirmation of the influence of veins can be seen in Fig. 6: As seen in previous work about SWI phase, venous vessels produce a phase effect due to dephasing between veins and surrounding tissue. This extravascular phase effect around a vessel has a very specific cross-shaped pattern with two positive and two negative lobes. If the blood's susceptibility changes during activation also the extravascular phase changes and the lobes either become less positive

or less negative leading to both positive and negative phase changes. See Fig. 5c where (tubular shaped) phase changes can be seen for some activated regions that are also seen in the magnitude. This phase information can be used to estimate oxygen saturation and its change during activation. In addition to the extravascular effect also the intravascular dephasing changes the phase of a voxel containing blood and tissue. In cortical tissue when only small intravascular veins are present the extravascular phase effect averages out. Also the intravascular dephasing effect will be very small, assuming a random distribution of vessel orientations it would be about 1/12 of the phase effect of a single vessel with the same blood volume. Because the venous blood volume in gray matter is very small (2%-3%) a phase change in grey matter is difficult to show experimentally. However, a very small phase effect was seen in an animal study [34] and in a whole brain analysis during breathing challenges [36].

[Figure 6 about here]

As has been previously described, the reconstructed data in fMRI are complex-valued, thus containing magnitude and phase values. The phase half of the data is generally discarded in fMRI analysis and activations are computed using statistical methods on only the magnitude half of the data. However, the phase component of the data contains important spatio-temporal biological information. It has been shown that the phase portion of the MRI data contains anatomical information through space [20,37] and functional information through time [27,35,38]. This functional information through time is about the local vasculature contained within a voxel. It is well accepted and has been experimentally verified that the magnetic fields

in and around vessels can be modeled [39]. Springer and Xu [39] find the vascular magnetic field $B_z(r,\phi,\xi)$ to be

$$B_z(r,\phi,\xi) = \begin{cases} 2\pi\Delta\chi B_0 Hct(1-Y)(3\cos^2\xi - 1)/3, & r \le a \\ 2\pi\Delta\chi B_0 Hct(1-Y)(a/r)^2 \sin^2\xi\cos 2\phi, & r > a \end{cases},$$ [4]

where r is the distance between the point of interest and the center of the cylinder cross-section in the plane normal to the cylinder, ϕ is the angle between r and the component of the main magnetic field B_0 in the plane, ξ is the angle between the applied magnetic field B_0 and the cylinder axis, $\Delta\chi$ is a susceptibility difference between fully oxygenated and fully deoxygenated red blood cells, Hct is the hematocrit level, Y is the oxygenation level of the blood, and a is the vessel radius. A reasonable value for the susceptibility difference is $\Delta\chi$=0.18 ppm [40] and for the hematocrit is Hct=0.4 [41]. The spins at location (r,ϕ,ξ) accumulate a different phase due to the additional the magnetic field $B_z(r,\phi,\xi)$. When using a gradient echo imaging pulse sequence with echo time TE, this phase accumulation is $\psi(r,\phi,\xi)= \bar{\gamma} \cdot B_z(r,\phi,\xi)\cdot$TE where $\bar{\gamma} =2\pi \cdot 42.58$ rad·MHz/T. Thus, a change in oxygenation level ΔY will produce a change in phase $\Delta\psi$ assuming all other parameters are held fixed.

In voxels that contain mainly parenchymal tissue where firing neurons are present, the vessels are small and randomly oriented, thus producing no coherent task related phase change. In voxels that are further down stream in the venous architecture that is more removed from the site of neuronal firing, the vessels are larger and well oriented, thus producing a coherent task related phase change. Down stream venous effects are apparent several millimeters away from the locus of activation [17]. Thus the phase component of the data contains information regarding the venous structure. It should be noted that the phase may also contain other physiological signal

[42]. In fMRI, statistical activation methods have predominantly utilized only the magnitude portion of the data, but more recently activation methods have been developed to utilize the entire complex-valued (magnitude and phase) data. A goal in fMRI has been to utilize the phase information in order to suppress or bias against determining voxels as active when they have task related phase changes. The reasoning is that voxels with task related phase changes are delocalized from the site of neuronal firing [27-30].

Removing the vein contribution in fMRI with a common spatial resolution by including the phase information

A subject was imaged using a susceptibility weighted high resolution flow compensated gradient recalled echo anatomic scan as described in Imaging Protcol 2 in Appendix B. A venogram was created by creating by taking a minimum intensity projection through several slices. The subject then performed a blocked design visual task of fixation on a mark and observing a flickering checkerboard. Activations are computed as described in Appendix A with the usual magnitude-only model in Eqn. 12 and the complex constant phase model in Eqn. 10 with $\theta_t=\theta$. Signed z-statistics are generated with an $\alpha=0.05$ slice-wise Bonferroni adjusted threshold.

The results for one slice are presented in Fig. 7. In Fig. 7(a) is a minimum intensity projection venogram through the shown functional slice and its neighboring slices. In Fig. 7(b) the magnitude-only activations are presented while in Fig. 7(c) the complex constant phase activations are presented. Venous activations are indicated with the identically located arrows.

[Figure 7 about here]

This shows that the phase component of the data contains important spatio-temporal biological information. This information can be used to remove or bias against less desirable voxels that contain larger venous vessels that are further removed from the site of neuronal firing. Statistical methods can be successfully utilized to bias against these larger venous vessels. In the simulation on ideal data, the complex constant phase model retains the power of the magnitude-only method at low CNRs when little to no TRPCs are present but biases against declaring voxels as active that have low CNR and larger TRPCs. As the CNR increases when TRPCs are present, the complex constant phase model transitions to behave similarly in terms of detection power to the magnitude-only model. These are favorable properties that an activation models should have. However, the complex constant phase model could possibly including some draining vein activations (large CNR) with large TRPCs. It should also be noted that in additional simulations (not shown) the larger the SNR, the larger the bias against voxels with task related phase changes. In the real data, the magnitude-only model detects four primary regions of focal activation. Three of the four areas identified in the venogram denoted by the blue arrows match hypo-intense areas in the venogram strongly indicate that they contain large venous structures. The complex constant phase model detects a subset of the magnitude-only activations as has been previously suggested [43]. The two of the three activation regions corresponding to hypo-intense venogram areas are completely eliminated while the third is nearly eliminated with the complex constant phase model. The single activation region that does not correspond to a hypo-intense area in the venogram is not eliminated and is strongly believed to be parenchymal in origin.

It has additionally been reported that magnitude-only and complex constant phase activations in fMRI data utilizing a spin echo pulse sequence are quite similar [44]. This suggests that the spin echo pulse sequence's suppression of BOLD contributions from large veins results in signal from the capillary bed that is already at constant phase. Thus, the complex constant phase model which assumes constant phase and the magnitude-only model both result in similar activation. Additionally, the complex constant phase model implemented on a gradient echo image yields results which are similar to both magnitude and complex constant phase model activations in spin echo images. This suggests that the complex constant phase model biases against the phase contributions from larger venous vessels and returns activation from the parenchymal capillary bed. The strong correlation of magnitude-only BOLD activations with large draining veins is in agreement with many studies [45].

It is clear that the complex constant phase method finds vastly reduced venous activations. It is also possible that non-task related phase changes may be responsible for the decreased volume of parenchymal activation found by the complex constant phase method. This could also be from un-resolved, well-oriented draining veins within the volume. It should also be noted that a parallel line of research to directly detect magnetic field changes due to neuronal firing has developed that utilizes the phase portion of the voxel time series in addition to the magnitude portion. At the present, magnetic field changes in wire phantoms have been detected [46] while human results are not yet conclusive [47].

From the aforementioned work, it is clear that the phase portion of the data that is generally discarded includes important biological information. This biological information can be used to

increase the focality of fMRI activation to the parenchymal tissue [48]. In the future, the use of the phase half of the data should become regular practice.

APPENDIX

Appendix A: Modeling and Detection

It is well known that thermal noise contributes statistically independent additive Gaussian noise in the real and imaginary channels of voxel measurements [43]. Assuming that this noise dominates, let a voxel contain true magnitude signal intensity ρ and phase angle θ. The resulting real channel measurement is $y_R = \rho\cos\theta + \eta_R$ and imaginary channel measurement is $y_I = \rho\sin\theta + \eta_I$, where η_R and η_I are statistically independent Gaussian noise with zero mean and variance σ^2. The real and imaginary voxel measurements can be viewed as a bivariate voxel measurement

$$\begin{pmatrix} y_R \\ y_I \end{pmatrix} = \begin{pmatrix} \rho\cos\theta \\ \rho\sin\theta \end{pmatrix} + \begin{pmatrix} \eta_R \\ \eta_I \end{pmatrix},$$
[5]

where the measurement errors are normally distributed, $(\eta_R\ \eta_I)' \sim N(0,\sigma^2 I_2)$. The joint (bivariate) distribution of y_R and y_I is given by

$$p(y_R, y_I \mid \rho,\theta,\sigma^2) = \frac{1}{\sqrt{2\pi\sigma^2}}\exp\left[-\frac{(y_R - \rho\cos\theta)}{2\sigma^2}\right] \cdot \frac{1}{\sqrt{2\pi\sigma^2}}\exp\left[-\frac{(y_I - \rho\sin\theta)}{2\sigma^2}\right].$$
[6]

Upon conversion from Cartesian coordinates to polar coordinates, the joint distribution of the magnitude m and phase φ is given by

$$p(m,\varphi \mid \rho,\theta,\sigma^2) = \frac{m}{2\pi\sigma^2}\exp\left\{-\frac{1}{2\sigma^2}\left[m^2 + \rho^2 - 2\rho m\cos(\varphi - \theta)\right]\right\}.$$
[7]

Generally only the magnitude portion of the data is used and the phase portion is discarded. When using only the magnitude portion, the joint distribution of the magnitude and phase needs

to be integrated with respect to the phase, φ, to produce the Ricean distribution [43,49,50] given by

$$p(m \mid \rho,\sigma^2) = \frac{m}{\sigma^2}\exp\left\{-\frac{m^2+\rho^2}{2\sigma^2}\right\}\int_{\varphi=-\pi}^{\pi}\frac{1}{2\pi}\exp\left\{\frac{\rho m}{\sigma^2}\cos(\varphi-\theta)\right\}d\varphi, \tag{8}$$

where the integral factor often denoted by $I_0\left(\rho m/\sigma^2\right)$ is the zeroth ordered modified Bessel function of the first kind. The population mean $E(m \mid \rho,\sigma^2)$ and variance $\mathrm{var}(m \mid \rho,\sigma^2)$ for the magnitude from the Rice distribution in Eqn. 5 do not have a simple form but the second moment is $E(m^2 \mid \rho,\sigma) = 2\sigma^2 + \rho^2$. If the signal-to-noise ratio (SNR) defined as SNR=ρ/σ, is "large," then Eqn. 5 becomes the normal distribution with $E(m \mid \rho,\sigma^2) = \sqrt{\rho^2 + \sigma^2}$ and $\mathrm{var}(m \mid \rho,\sigma^2) = \sigma^2$. If the SNR is zero, then Eqn. 8 becomes the Rayleigh distribution [51] with population mean $E(m \mid \rho,\sigma^2) = \sigma\sqrt{\pi/2}$ and variance $\mathrm{var}(m \mid \sigma^2) = \sigma^2(2 - \pi/2)$.

Similar to discarding the phase and analyzing the magnitude, one can discard the magnitude and analyze the phase. When using only the phase portion, the joint distribution of the magnitude and phase needs to be integrated with respect to the magnitude m to produce the marginal phase distribution

$$p(\varphi \mid \rho,\theta,\sigma^2) = \frac{1}{2\pi}\exp\left\{-\frac{\rho^2}{2\sigma^2}\right\}\left[1 + \frac{\rho\sqrt{2\pi}}{\sigma}\cos(\varphi-\theta)\exp\left\{\frac{\rho^2\cos(\varphi-\theta)}{2\sigma^2}\right\}\Phi\left(\frac{\rho^2\cos(\varphi-\theta)}{\sigma}\right)\right], \tag{9}$$

where Φ is the standard normal cumulative distribution function. The population mean $E(\varphi \mid \rho,\theta,\sigma^2)$ and variance $\mathrm{var}(\varphi \mid \rho,\theta,\sigma^2)$ from the marginal phase distribution in Eqn. 9 do not have a simple form and must be determined numerically. If the SNR is "large," Eqn. 9 becomes the normal distribution with population mean $E(\varphi \mid \rho,\theta,\sigma^2) = \theta$ and

$var(\varphi \mid \rho, \theta, \sigma^2) = (\sigma / \rho)^2$. If the SNR is zero, then Eqn. 9 becomes the uniform distribution

$p(\varphi) = 1/(2\pi)$. The population mean for the phase from the uniform distribution should not exist

as all directions are equally likely. The mean of this uniform distribution is an artifact of the

choice of axis. If $\varphi \in (-\pi, \pi]$, the population mean is $E(\varphi) = 0$ while if $\varphi \in [0, 2\pi)$, the

population mean is $E(\varphi) = \pi$. Regardless of the choice of axis, $var(\varphi) = \pi^2 / 3$.

In fMRI, voxel measurements are taken over time and thus it is necessary to model temporal

drifts in the magnitude and/or phase. Also of interest is to detect particular changes in the

magnitude and/or phase termed activation. Following the same specifications as in Eqn. 2, the

observed complex-valued voxel time series data (real part y_R stacked above imaginary part y_I)

can be described as before with the magnitude ρ_t and the phase, θ_t at time t, $t=1,...,n$ as

$$\begin{pmatrix} y_{Rt} \\ y_{It} \end{pmatrix} = \begin{pmatrix} \rho_t \cos \theta_t \\ \rho_t \sin \theta_t \end{pmatrix} + \begin{pmatrix} \eta_{Rt} \\ \eta_{It} \end{pmatrix} \qquad [10]$$

with normally distributed measurement errors, $(\eta_{Rt}, \eta_{It})' \sim N(0, \sigma^2 I_2)$. As previously described, the

phase portion of the data in fMRI analysis is generally discarded. Upon discarding the phase

portion of the data, the observed magnitude m_t follows the Ricean distribution with underlying

true magnitude ρ_t. The true underlying magnitude is then modeled

as $\rho_t = x_t'\beta = \beta_0 + \beta_1 x_{1t} + \cdots + \beta_{q1} x_{q1t}$ where x_t' is the tth row of a magnitude design matrix X and β

is a is a q_1 dimensional vector of magnitude regression coefficients. When utilizing the

magnitude-only time series the Ricean distribution should be used to form the likelihood and log

likelihood for the parameters [52]

$$LL(\beta, \sigma^2) = -n \log \sigma^2 + \sum_{t=1}^{n} \log m_t - \frac{1}{2\sigma^2} \left(\sum_{t=1}^{n} m_t^2 + \sum_{t=1}^{n} (x_t'\beta)^2 \right) + \sum_{t=1}^{n} \log I_0 \left(\frac{x_t'\beta \cdot m_t}{\sigma^2} \right) . \qquad [11]$$

From Eqn. 11 maximum likelihood estimates of the parameters (β, σ^2) can be determined numerically for both restricted null and unrestricted alternative hypotheses using Lagrange constraints. For example with unrestricted null and alternative hypotheses H_0: $C\beta = \tau$ vs. H_1: $C\beta \neq \tau$, where C is a full row rank matrix with the hypotheses to be tested in the form of linear constraints in the rows and τ is a column vector of dimension equal to the full row rank of C.

The log likelihood expression in Eqn. 11 is rarely, if ever, used. A large SNR normal approximation to the Ricean distribution is generally used. The normal approximation is used because estimation of the parameters in Eqn. 11 requires numerical maximization and because in fMRI the SNR within the object being imaged is generally assumed to be high enough to justify the normal approximation. With the use of the normal approximation, the usual general linear model

$$m_t = x_t'\beta + \varepsilon_t \qquad [12]$$

can be used where the measurement error $\varepsilon_t \sim N(0, \sigma^2)$. However, an approximation has been developed [52] using the first two terms of a Taylor series for the cosine term in I_0 to obtain

$$p(m_t \mid \beta, \sigma^2) = \frac{1}{\sqrt{2\pi\sigma^2}} \sqrt{\frac{m_t}{x_x'\beta}} \exp\left\{ -\frac{(m_t - x_t'\beta)^2}{2\sigma^2} \right\}. \qquad [13]$$

A likelihood can be formulated from Eqn. 13 and parameters estimated from it. Additionally, it has been shown by using the full complex data model in Eqn. 7 that the magnitude-only model in Eqn. 8 is equivalent to a complex data model where the phase is unrestricted ($\theta_t \neq \theta_{t'}$, $t \neq t'$) and estimated at each time point in each voxel [53]. Regardless of the magnitude-only model that is used, the phase portion of the data is not utilized.

Similar to discarding the phase portion of the data and analyzing the magnitude-only time series, one can discard the magnitude portion and analyze the phase-only time series. Upon discarding the magnitude portion of the data, the observed phase φ_t at time t follows the marginal distribution of Eqn. 9 with underlying true phase θ_t and magnitude ρ_t. The true underlying phase is then modeled as $\theta_t = u_t'\gamma = \gamma_0 + \gamma_1 u_{1t} + \cdots + \gamma_{q2} u_{q2t}$ where u_t' is the tth row of a phase design matrix U and γ is a q_2 dimensional vector of phase regression coefficients. When utilizing the phase-only time series the marginal distribution of Eqn. 9 should be used to form the likelihood and log likelihood for the parameters [54]

$$
\begin{aligned}
LL(\gamma,\beta,\sigma^2) = &-n\log(2\pi) - \frac{1}{2\sigma^2}\sum_{t=1}^{n}(x_t'\beta)^2 \\
&+ \sum_{t=1}^{n}\log\left[1 + \frac{x_t'\beta\sqrt{2\pi}}{\sigma}\cos(\varphi_t - u_t'\gamma)\exp\left\{\frac{(x_t'\beta)^2\cos(\varphi_t - u_t'\gamma)}{2\sigma^2}\right\}\Phi\left(\frac{(x_t'\beta)^2\cos(\varphi_t - u_t'\gamma)}{\sigma}\right)\right]
\end{aligned}
\qquad [14]
$$

From Eqn. 14 maximum likelihood estimates of the parameters (γ,β,σ^2) can in principle be determined numerically for both restricted null and unrestricted alternative hypotheses using Lagrange constraints. For example with unrestricted null and alternative hypotheses H$_0$: Dγ=δ vs. H$_1$: D$\gamma\neq\delta$, where D is a full row rank matrix with the hypotheses to be tested in the form of linear constraints in the rows and τ is a column vector of dimension equal to the full row rank of D.

The log likelihood expression in Eqn. 14 is rarely, if ever, used. A large SNR normal approximation to the marginal distribution of Eqn. 9 is generally used. The normal approximation is used because estimation of the parameters in Eqn. 14 requires numerical maximization and because in fMRI the SNR within the object being imaged is generally assumed to be high enough to justify the normal approximation. With the use of the normal approximation, the usual general linear model

$$\varphi_t = u_t'\gamma + \varepsilon_t \tag{15}$$

is used where the measurement error $\varepsilon_t \sim N(0, \sigma_{\varphi t}^2 = \sigma /(x_t'\beta))$. When using Eqn. 15, one needs to pay particular attention to phase transitions. Very often the phase-only time series is unwrapped and the usual GLM applied, however this can result in improper estimation of the regression coefficients and incorrect statistics [54].

The marginal phase distribution in Eqn. 9 can be approximated by the von Mises angular distribution for an angular regression model with an angular dependent variable and linear independent variable [54,55]. The von Mises distribution [56] has the following form

$$p(\varphi_t \mid \gamma, \kappa_t) = \frac{\exp(\kappa_t \cos(\varphi_t - u_t'\gamma))}{2\pi I_0(\kappa_t)} \tag{16}$$

with mean $\theta_t = u_t'\gamma$ and concentration $\kappa_t = m_t \cdot x_t'\beta / \sigma^2$ where $0 \le \kappa_t$ and $-\pi \le \varphi_t, \theta_t < \pi$. It is reasonable to assume that the variance is temporally constant so that $\kappa_t = \kappa$. A likelihood can be formulated from Eqn. 16 and parameters estimated from it. The von Mises distribution has a limiting normal distribution with mean θ_t and variance $1/\kappa$ when κ is large and tends to look like a normal distribution with its two tails tied together at the phase transition. With the use of the normal approximation, the usual general linear model in Eqn. 15 is used. Regardless of the phase-only model that is utilized, the magnitude portion of the data is not utilized.

[Figure 8 about here]

Complex-valued time series as presented in Fig. 8 have been modeled simultaneously in Eqn. 10 and thus we can fully utilize the complex-valued (magnitude and phase) data. From Eqn. 10,

maximum likelihood estimates of the parameters (β,γ, σ^2) can in principle be determined for both constrained null and unconstrained alternative hypotheses using Lagrange constraints. One example of possible unrestricted null and alternative hypotheses is H_0: $C\beta=\tau$,$D\gamma=\delta$ vs. H_1: $D\gamma\neq\delta$,$C\beta\neq\tau$ where all variables are as previously defined [28]. Model parameters are estimated under the constrained null hypothesis ($\tilde{\beta},\tilde{\gamma},\tilde{\sigma}^2$) and unconstrained alternative hypotheses ($\hat{\beta},\hat{\gamma},\hat{\sigma}^2$). These parameter estimates can be used to form a generalized likelihood ratio statistic λ and negative twice the log of λ is χ^2 distributed in large samples with degrees of freedom equal to the sum of number of rows in C and D. These several statistical fMRI activation models can be used to various detect changes in either the magnitude, the phase, or both the magnitude and phase. Since the distribution of the activation statistics in these models these models are not all the same under the null hypothesis, the significance of the models can be compared all on the $-\log_{10}$(p-value) scale. The detection power for the magnitude-only, phase-only, and complex constant phase (complex model with a constant phase denoted CCP) are presented in Fig. 9.

It seems natural that there is important biological information contained within the phase. This phase information can be used to reduce or bias against the declaration of a voxel as being active (having statistically significant task related magnitude changes). In what follows the method used by Nencka and Rowe [30] is used which is the model in Eqn. 10 where $\rho_t = x_t'\beta = \beta_0 + \beta_1 x_{1t} + \cdots + \beta_{q1} x_{q1t}$ but the phase is assumed to be temporally constant, $\theta_t = \gamma_0$ as in[43]. This model is termed the complex constant phase model. When task related phase changes are present, the complex constant phase model does not model these task related phase

changes. The unmodeled task related phase changes result in an increased residual variance and decreased activation statistics.

In Nencka and Rowe [30], the magnitude-only model [3,54], the phase-only model [54], and the complex constant phase model [43] were examined with simulated data in order to characterize their activation properties. The simulated data was generated using Eqn. 10 with $q_1=q_2=2$. The regression coefficients β_0, β_2, and γ_2, were set to determine the temporal signal-to-noise ratio (SNR=β_0/σ), temporal contrast-to-noise ratio (CNR=β_2/σ), and task-related phase change (TRPC=$\gamma_2 \cdot 180/\pi$). The remaining coefficients were $\beta_1=0$, $\gamma_0=\pi/6$, and $\gamma_1=0$. Time courses for each element of a 128×128 array were created using the complex-valued general linear model defined in Eqn. 10. The regression coefficients were varied in equal steps, $\beta_2=0$ to σ and $\gamma_2=0$ to $5\pi/180$. In each element of the array random normally distributed noise variates were added with $\sigma=1$ in the real and imaginary components and a temporal SNR of 20. This temporal SNR approximately corresponds to the SNR measured in the human data they presented. One thousand simulated data sets were generated and the three models were applied to determine their detection for an $\alpha=0.05$ Bonferroni adjusted threshold [57,58].

This simulation was replicated and the results are shown in Fig. 9. The horizontal axis displays the temporal CNR, as it varies from 0 to 1, and the vertical axis presents the TRPC as it changes from 0 to 5 degrees. As expected, the power surface in Figs. 9(a) shows that the magnitude-only model depends solely on the temporal CNR and the power surface in Figs. 9(b) shows that the phase-only model depends solely on the TRPC. The power surface in Fig. 9(c) shows that the complex constant phase model depends upon both the CNR and TRPC. When the TRPC is small, the complex constant phase method performs like the magnitude-only method declaring voxels

with significant CNRs active with high power. These TRPC–CNR combinations are observed in gray matter parenchymal voxels where neurons are present and detection is desirable. However, as the TRPC increases, the similarity between the magnitude-only and complex constant phase statistical methods diminishes [59]. When larger TRPCs are present in the time series, the complex constant phase method requires a higher CNR in order to declare voxels active. In the brain, voxels with moderate CNRs and larger TRPCs include those which contain draining veins that are undesirable. Thus, the complex constant phase method biases against voxels which may contain draining veins. If a voxel contains both a large TRPC and CNR, the constant phase method declares the voxel active similar to the magnitude-only model and does not bias against the contaminated voxels. This suggests that the complex constant phase method may bias against some voxels with TRPCs while not removing all of them.

Appendix B: Imaging protocols

B.1: Imaging Protocol of high resolution fSWI

Experiments were performed on a 3 T Siemens Magnetom Trio (Siemens, Erlangen, Germany) using a custom-built eight-channel array forming a strip along the visual cortex from left to right (Stark Contrast; MRI Coils, Erlangen, Germany). The subjects were positioned comfortably but firmly using cushions between the cover of the coil and the ears to minimize head motion. Functional datasets were obtained using a 3D, first-order flow-compensated gradient-echo FLASH sequence. The 3D slab was acquired using: TR=35 ms; TE=28 ms; flip angle=158; bandwidth=100 Hz/pixel; field of view=144×108 mm^2; slab thickness=30 mm. The TE was chosen to optimise vein visibility [21]. GRAPPA (generalized auto-calibrating partially parallel acquisitions) [60] was used as the parallel imaging mode with an acceleration factor of 2 or 4 and

24 reference lines. Acceleration was performed in the in-plane phase encoding direction (left–right), i.e. following the strip of the coil elements. An isotropic spatial resolution of $0.75 \times 0.75 \times 0.75$ mm^3 (0.42 mL) was used. A 192×144 matrix with either 20 or 40 slices of 0.75 mm thickness were used. The 3D slab orientation was axial and tilted towards coronal to be parallel to the calcarine sulcus (see Fig. 3a). In most cases the resulting (volume) acquisition times was 50 s but could be longer (up to 118 s) depending on the number of slices and the acceleration factor used, respectively. Anatomical datasets were obtained using a magnetization-prepared rapid gradient echo (MP-RAGE) sequence with the following imaging parameters: TR=2300; inversion time=1100 ms; TE=8 ms; flip angle=88 degrees; acquisition time=6 min. The geometrical parameters were identical with the high-resolution functional scan (field of view=144×108 mm^2; spatial resolution=$0.75 \times 0.75 \times 0.75$mm^3) except that 80 slices were acquired.

The stimulus paradigm consisted of a block showing a black screen with a fixation cross interleaved with a block showing a flickering checkerboard (5 Hz, i.e. 200 ms for the full cycle). The block duration was matched to the respective acquisition times per 3D volume. These blocks were repeated between 14 to 37 times resulting total acquisition times between 15 min to 30 per run. The data were analyzed using the general linear model as implemented in FEAT [62]. FSL MCFLIRT was used for motion correction between the volumes of the functional dataset. No spatial or temporal smoothing was used. Veins are easily identified as dark spots or lines as shown in Fig. 3b as a result of dephasing between blood and tissue compartments in a voxel and extravascular effects [62,63]. Veins could therefore be segmented manually in the functional datasets based on their appearance, but we have developed an automatic procedure [64]) that makes manual tracing obsolete. A segmented venous vascular tree can be seen in Fig. 4a

(middle) which was performed manually using the software package MRIcro 1.39b4 [65]. A region of interest containing these segmented venous vessels is used as a mask to remove the respective voxels in the functional dataset. In a second step, the general linear model will be applied again to these datasets with these visible veins removed. For visualization purposes the resulting z-maps were smoothed. Activated volumes are quantified before and after application of the venous mask by using all pixels in the z-maps above a threshold Z=2 and a cluster threshold of P=0.005.

B.2: Imaging protocol of standard resolution fMRI experiment using complex data

To examine the properties of the magnitude-only and constant phase activation models in real data. This includes the bias of the complex constant phase model against declaring voxels as active that potentially contain larger vessels [66]. A subject was imaged using a 3.0 T GE Signa LX scanner. The subject was presented a flashing checkerboard visual stimulus while a gradient-echo EPI pulse sequence was utilized to obtain fMRI data. A venogram of the visual cortex was also performed using a susceptibility weighted, high resolution, flow compensated, gradient recalled echo scan. The parameters for this venographic pulse sequence included: TE= 28 ms, TR=46 ms, FA=20 degrees, field of view $24\times18\times6$ cm^3, acquisition matrix $512\times256\times60$. Venograms were created by minimum intensity projections through multiple slices [20]. The subject then performed a blocked design visual task of fixation on a mark then observing a checkerboard flickering at 4 Hz. The task included an initial rest period of 20 seconds followed by eight epochs of 16 seconds of task and 16 seconds of rest. The parameters for this functional experiment included: TE=45.3 ms, TR=2000 ms, FA=77 degrees, field of view 24×24 cm^2, in-plane acquisition matrix 96×96, slice thickness 2.5 mm.

REFERENCES

1. Ogawa S, Lee TM, Kay AR, Tank DW. Brain magnetic resonance imaging with contrast dependent on blood oxygenation. Proceedings of the National Academy of Sciences of the United States of America 1990a;87:9868-9872.

2. Ogawa S, Lee TM, Nayak AS, Glynn P. Oxygenation-sensitive contrast in magnetic resonance image of rodent brain at high magnetic fields. Magnetic Resonance in Medicine 1990b;14:68-78.

3. Bandettini PA, Jesmanowicz A, Wong EC, Hyde JS. Processing strategies for time-course data sets in functional MRI of the human brain. Magn. Reson. Med. 1993;30:161-173.

4. Hoge RD, Atkinson J, Gill B, Crelier GR, Marrett S, Pike GB. Investigation of BOLD signal dependence on cerebral blood flow and oxygen consumption: the deoxyhemoglobin dilution model. Magn Reson Med 1999;42: 849-863

5. Grubb RL Jr, Raichle ME, Eichling JO, Ter-Pogossian MM. The effects of changes in $PaCO_2$ on cerebral blood volume, blood flow, and vascular mean transit time. Stroke 1974;5:630-639

6. van Zijl PC, Eleff SM, Ulatowski JA, Oja JM, Ulug AM, Traystman RJ, Kauppinen RA. Quantitative assessment of blood flow, blood volume and blood oxygenation effects in functional magnetic resonance imaging. Nat Med 1998;4:159-167.

7. Lai S, Hopkins AL, Haacke EM, Li D, Wasserman BA, Buckley P, Friedman L, Meltzer, H, Hedera P, Friedland R. Identification of vascular structures as a major source of signal contrast in high resolution 2D and 3D functional activation imaging of the motor cortex at 1.5T: preliminary results. Magn Reson Med 1993;30:387-392.

8. Frahm J, Merboldt KD, Hanicke W, Kleinschmidt A, Boecker H. Brain or vein--oxygenation or flow? On signal physiology in functional MRI of human brain activation. NMR Biomed 1994;7:45-53.

9. Segebarth C, Belle V, Delon C, Massarelli R, Decety J, Le Bas JF, Decorps M, Benabid, AL. Functional MRI of the human brain: predominance of signals from extracerebral veins. Neuroreport 1994;5:813-816.

10. Barth M, Reichenbach JR, Venkatesan R, Moser E, Haacke EM. High-resolution, multiple gradient-echo functional MRI at 1.5 T. Magn Reson Imaging 1999;17; 321-329.

11. Hoogenraad FG, Hofman MB, Pouwels PJ, Reichenbach JR, Rombouts SA, Haacke, EM. Sub-millimeter fMRI at 1.5 Tesla: correlation of high resolution with low resolution measurements. J Magn Reson Imaging 1999;9:475-482.

12. Hoogenraad FG, Pouwels PJ, Hofman MB, Reichenbach JR, Sprenger M, Haacke EM. Quantitative differentiation between BOLD models in fMRI. Magn Reson Med 2001;45:233-246.

13. Barth M, Norris DG. Very high-resolution three-dimensional functional MRI of the human visual cortex with elimination of large venous vessels. NMR Biomed 2007; 20:477-484.

14. Oja JM, Gillen J, Kauppinen RA, Kraut M, van Zijl PC. Venous blood effects in spin-echo fMRI of human brain. Magn Reson Med 1999;42:617-626.

15. Duvernoy HM, Delon S, Vannson JL. Cortical blood vessels of the human brain. Brain Res Bull 1981;7:519-579.

16. Yamaguchi S, Yamakawa T, Niimi H. Red cell velocity and microvessel diameter measurement by a two fluorescent tracer method under epifluorescence microscopy: application to cerebral microvessels of cats. Int J Microcirc Clin Exp 1992;11:403-416.

17. Turner R. How much cortex can a vein drain? Downstream dilution of activation-related cerebral blood oxygenation changes. Neuroimage 2002;16:1062-1067.

18. Lauwers F, Cassot F, Lauwers-Cances V, Puwanarajah P, Duvernoy H. Morphometry of the human cerebral cortex microcirculation: general characteristics and space-related profiles. Neuroimage 2008;39:936-948.

19. Boxerman JL, Bandettini PA, Kwong KK, Baker JR, Davis TL, Rosen BR, Weisskoff, RM. The intravascular contribution to fMRI signal change: Monte Carlo modeling and diffusion-weighted studies in vivo. Magn Reson Med 1995;34:4-10.

20. Reichenbach JR, Venkatesan R, Schillinger DJ, Kido DK, Haacke EM. Small vessels in the human brain: MR venography with deoxyhemoglobin as an intrinsic contrast agent. Radiology 1997;204:272-277.

21. Reichenbach JR, Barth M, Haacke EM, Klarhofer M, Kaiser WA, Moser E. High-resolution MR venography at 3.0 Tesla. J Comput Assist Tomogr 2000;24:949-957.

22. Dashner RA, Clark DL, Kangarlu A, Baudendistel KT, Chakeres DW. Epoxy-resin injection of the cerebral arterial microvasculature: An evaluation of the limits of spatial resolution in 8 Tesla MRI. Clin Anat 2005;18;164-170.

23. Ogawa S, Menon RS, Tank DW, Kim SG, Merkle H, Ellermann JM, Ugurbil K. Functional brain mapping by blood oxygenation level-dependent contrast magnetic resonance imaging. A comparison of signal characteristics with a biophysical model. Biophysical Journal 1993;64:803-812.

24. Diemling M, Barth M, Moser E. Quantification of signal changes in gradient recalled echo FMRI. Magn Reson Imaging 1997;15;753-762.

25. Yacoub E, Van De Moortele PF, Shmuel A, Ugurbil K. Signal and noise characteristics of Hahn SE and GE BOLD fMRI at 7 T in humans. Neuroimage 2005;24:738-750.

26. Cheng K, Waggoner RA, Tanaka K. Human ocular dominance columns as revealed by high-field functional magnetic resonance imaging. Neuron 2001;32:359-374.

27. Menon RS. Postacquisition suppression of large-vessel BOLD signals in high-resolution fMRI. Magn Reson Med 2002;47:1-9.

28. Rowe DB. Modeling both the magnitude and phase of complex-valued fMRI data. Neuroimage 2005;25:1310-1324.

29. Rowe DB, Nencka AS. Complex activation suppresses venous BOLD in GE-EPI fMRI data. Proc Intl Soc Magn Reson Med 2006;14:2834.

30. Nencka AS, Rowe DB. Reducing the unwanted draining vein BOLD contribution in fMRI with statistical post-processing methods. Neuroimage 2007;37:177-188.

31. Song AW, Wong EC, Tan SG, Hyde JS. Diffusion weighted fMRI at 1.5 T. Magn Reson Med 1996;35:155-158.

32. Jochimsen TH, Norris DG, Mildner T, Moller HE. Quantifying the intra- and extravascular contributions to spin-echo fMRI at 3 T. Magn Reson Med 2004;52:724-732.

33. Michelich CR, Song AW, Macfall JR. Dependence of gradient-echo and spin-echo BOLD fMRI at 4 T on diffusion weighting. NMR Biomed 2006;19:566-572.

34. Cusack R, Mitchell DJ, Beauregard DA, Salfity MF, Huntley JM. Individual variability in cerebral vein structure and the BOLD signal. Proc Org Hum Brain Mapp, Florence(Italy) 2006, S99(#650 M-PM), pp. S99(#650 M-PM).

35. Zhao F, Jin T, Wang P, Hu X, Kim SG. Sources of phase changes in BOLD and CBV-weighted fMRI. Magn Reson Med 2007;57:520-527.

36. Sedlacik J, Kutschbach C, Rauscher A, Deistung A, Reichenbach JR. Investigation of the influence of carbon dioxide concentrations on cerebral physiology by susceptibility-weighted magnetic resonance imaging (SWI). Neuroimage 2008;43:36-43.

37. Duyn, JH, van Gelderen, P, Li T-Q, de Zewart JA, Koretsky AP, Fukunaga M. High field MRI of brain cortical substructure based on signal phase. PNAS 2007;104:11796-11801.

38. Hoogenraad FG, Reichenbach JR, Haacke EM, Lai S, Kuppusamy K, Sprenger M. In vivo measurement of changes in venous blood-oxygenation with high resolution functional MRI at 0.95 Tesla by measuring changes in susceptibility and velocity. Magn Reson Med 1998;39:97-107.

39. Springer CS, Xu Y. Aspects of bulk magnetic susceptibility in in vivo MRI and MRS. In Rink, PA, Muller, RN editors. New Developments in Contrast Agent Research. European Magnetic Resonance Forum, Blonay, Switzerland; 1991. p 13-25.

40. Weisskoff RM, Kiihne S. MRI susceptometry: image-based measurement of absolute susceptibility of MR contrast agent and human blood. Magn Reson Med 1992;24,375-383.

41. Guyton AC. Textbook of Medical Physiology. W.B. Saunders Company, Philadelphia 1981. p 206.

42. Pfeuffer J, Van de Moortele PF, Ugurbil K, Hu X, Glover GH. Correction of physiologically induced global off-resonance effects in dynamic echo-planar and spiral functional imaging. Mag Reson Med 2002;47:344-353.

43. Rowe DB, Logan BR. A complex way to compute fMRI activation. NeuroImage 2004;23, 1078-1092.

44. Nencka AS, Rowe DB. Complex constant phase method removes venous BOLD component in fMRI. Proc Intl Soc Magn Reson Med 2005;13:495.

45. Duong TQ, Yacoub E, Adriany G, Hu X, Uurbil K, Kim S-G. Microvascular BOLD contribution at 4 and 7 T in the human brain: Gradient-echo and spin-echo fMRI with suppression of blood effects. Magn Reson Med 2003;49:1019-1027.

46. Bodurka J, Jesmanowicz A, Hyde JS, Xu H, Estkowski L, Li S-J. Current-induced magnetic resonance phase imaging. J Magn Reson 1999;137:265-271.

47. Bandettini PA, Petridou N, Bodurka J. Direct detection of neuronal activity with MRI: Fantasy, possibility, or reality? Applied Magnetic Resonance 2005;29:65-88.

48. Rowe DB. Complex activation is more focal and concentrated to parenchymal tissue. Proc Intl Soc Magn Reson Med 2005;13:1575.

49. Rice SO. Mathematical analysis of random noise. Bell Syst Tech J 1944;23:282.

50. Gudbjartsson H, Patz S. The Rician distribution of noisy data. Magn Reson Med 1995;34:910-914.

51. Haacke EM, Brown R, Thompson M, Venkatesan R. Magnetic Resonance Imaging: Physical Principles and Sequence Design. John Wiley and Sons, New York, NY; 1999.

52. Rowe DB. Parameter estimation in the magnitude-only and complex-valued fMRI data models. Neuroimage 2005;25:1124-1132.

53. Rowe DB, Logan BR. Complex fMRI analysis with unrestricted phase is equivalent to a magnitude-only model. NeuroImage 2005;24:603-606.

54. Rowe DB, Meller CP, Hoffmann RG. Characterizing phase-only fMRI data with an angular regression model. J Neurosci Methods 2007;161:331-341.

55. Fisher NI, Lee AJ. Regression models for an angular response. Biometrics 1992;48:665-677.

56. Jammalamadaka SR, SenGupta. Topics in circular statistics. Singapore: World Scientific Publishing Co; 2001

57. Logan BR, Rowe DB. An evaluation of thresholding techniques in fMRI analysis. Neuroimage 2004;22:95-108.

58. Logan BR, Geliazkova MP, Rowe DB. An evaluation of thresholding techniques in fMRI analysis. Hum Brain Mapp, 2008;29:1379-1389.

59. Nencka AS, Rowe DB. Theoretical results demonstrate fundamental differences in venous BOLD reducing fMRI activation methods. Proc Intl Soc Magn Reson Med 2006;14:3269.

60. Griswold MA, Jakob PM, Heidemann RM, Nittka M, Jellus V, Wang J, Kiefer B, Haase A. Generalized autocalibrating partially parallel acquisitions (GRAPPA). Magn Reson Med 2002;47:1202–1210.

61. FSL, FMRIB, Oxford, UK; http://www.fmrib.ox.ac.uk/fsl

62. Reichenbach JR, Essig M, Haacke EM, Lee BC, Przetak C, Kaiser WA, Schad LR. High-resolution venography of the brain using magnetic resonance imaging. Magma 1998;6: 62–69.

63. Reichenbach JR, Haacke EM. High-resolution BOLD venographic imaging: a window into brain function. NMR Biomed. 2001;14:453–467.

64. Koopmans PJ, Manniesing R, Norris DG, Viergever M, Niessen WJ, Barth M. Vein segmentation from 3D HIGH RESOLUTION MR venograms by using vessel enhancing diffusion. Proceedings of the ESMRMB, Warsaw, 2006; p 361.

65. Rorden C. http://www.sph.sc.edu/comd/rorden/ mricro.html

66. Nencka AS, Paulson ES, Rowe DB. Complex constant phase model reduces venous contributions to BOLD cortical activations in the visual cortex. Proc Intl Soc Magn Reson Med 2008;16:2338.

TABLES

Type of vessels	Velocity (mm/s)	Diameter (um)
Capillaries	0.26-1.1	< 10
Venules	0.18-4.2	10-60
Intracortical veins	> 5	> 60
Pial veins		25 – 250

Table 1: Data are taken from measurements of cat cortex (Yamaguchi et al., 1992) and are consistent with estimates for human brain vessels given in textbooks of physiology (see e.g. Guyton AC (ed.) (1991) Textbook of Medical Physiology, 8th edn., Philadelphia: W.B. Saunders Company).
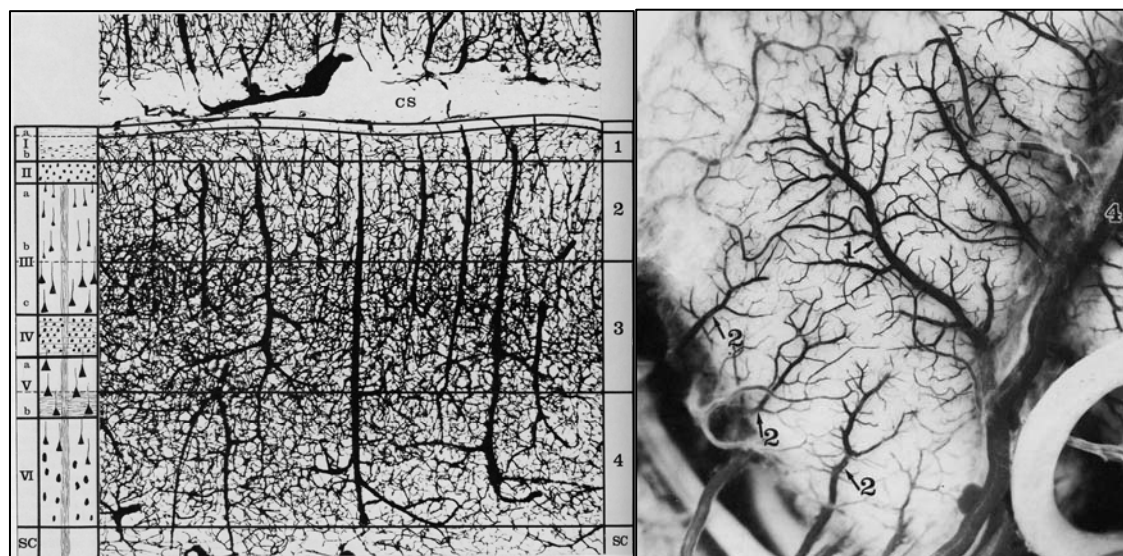
FIGURES

Figure 1. Vascular architecture of the cortex. (a) On the left side the classification of the cortical layers (I-VI), on the right hand side the vascular layers (1-4) are given. (b) View on the cortical surface depicting the extracortical pial vein network. Reprinted from Duvernoy et al. (1981).
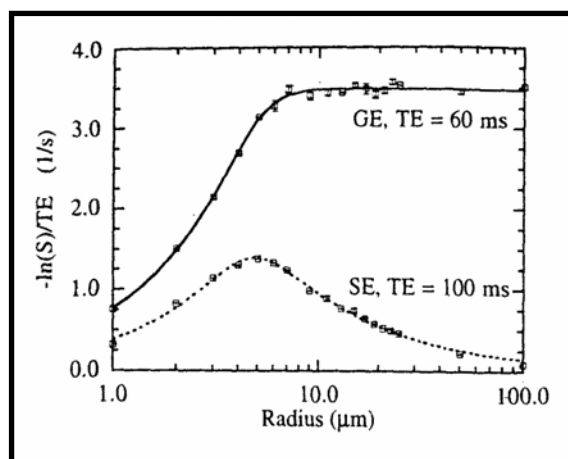
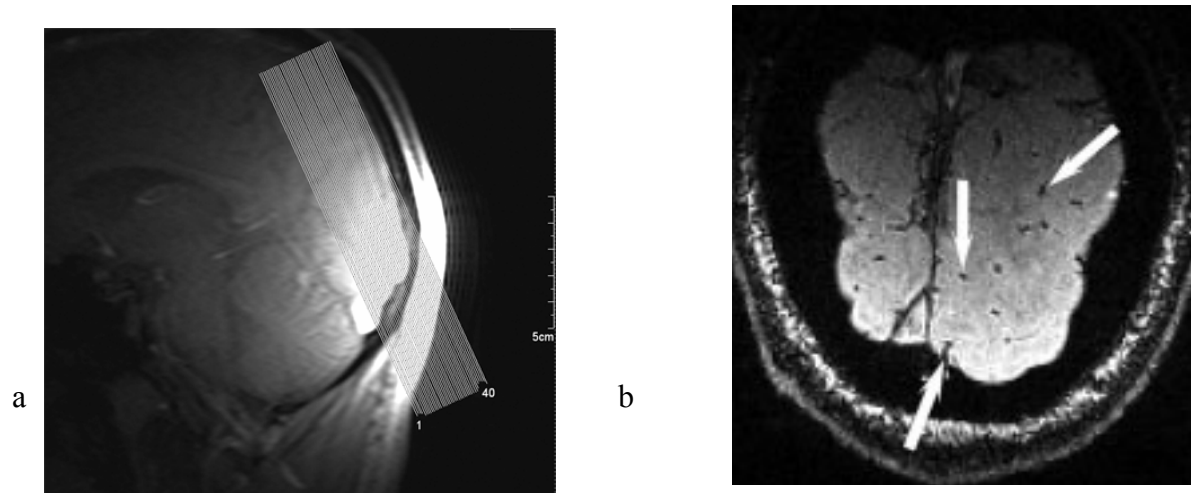**Figure 2.** Gradient and spin echo signals as a function of vessel radius. Reprinted from Boxerman et al. (1995).

Figure 3. a) Positioning of the 3D slab. b) Single slice out of functional data set (0.75 mm voxel size). Note the clear depiction of venous vessels.
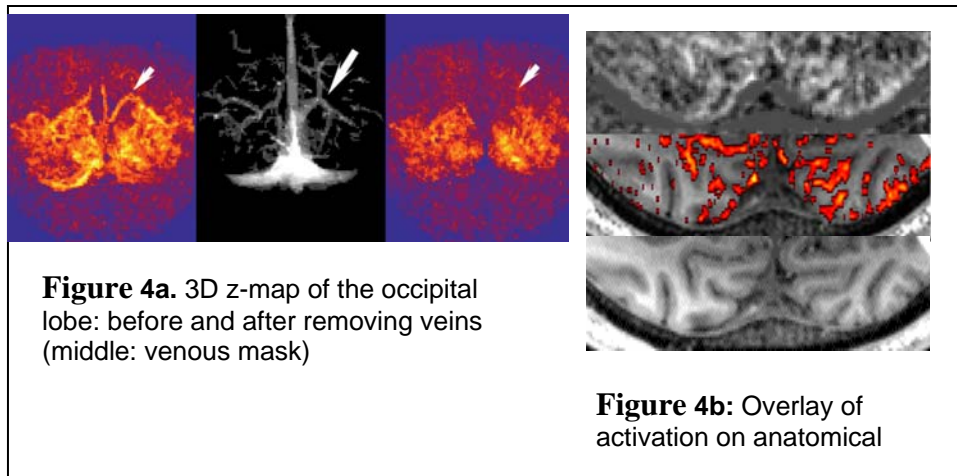
Figure 4a. 3D z-map of the occipital lobe: before and after removing veins (middle: venous mask)
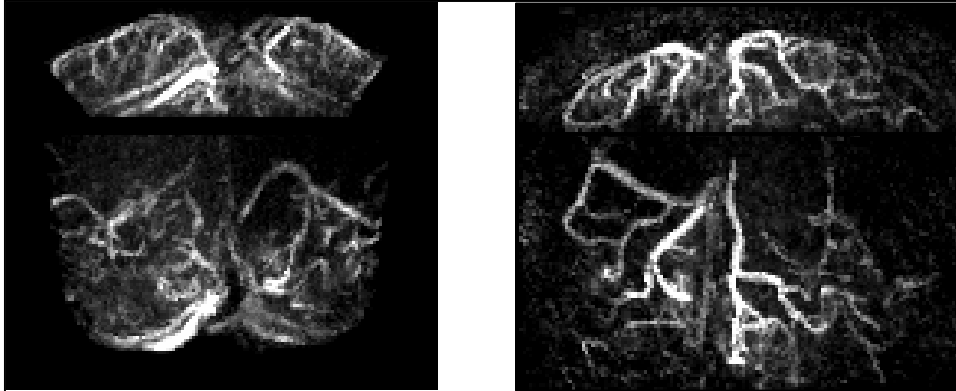
Figure 4b: Overlay of activation on anatomical

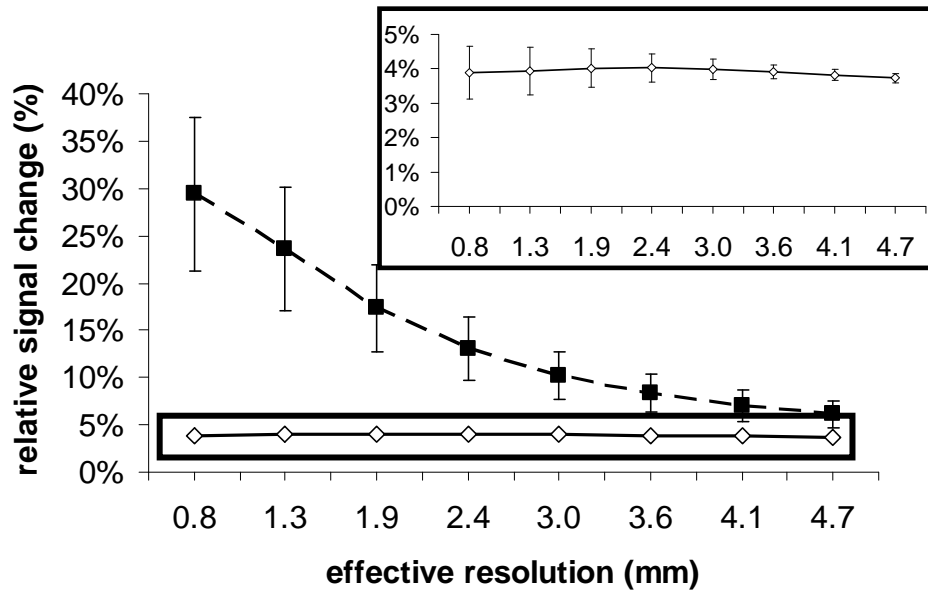**Figure 4c.** Signal change map of two different subjects

Figure 5a. Relative signal change of a cortical (gray matter) region (open diamonds) and of a venous region (full squares). Insert shows the enlarged signal change of the cortical ROI.
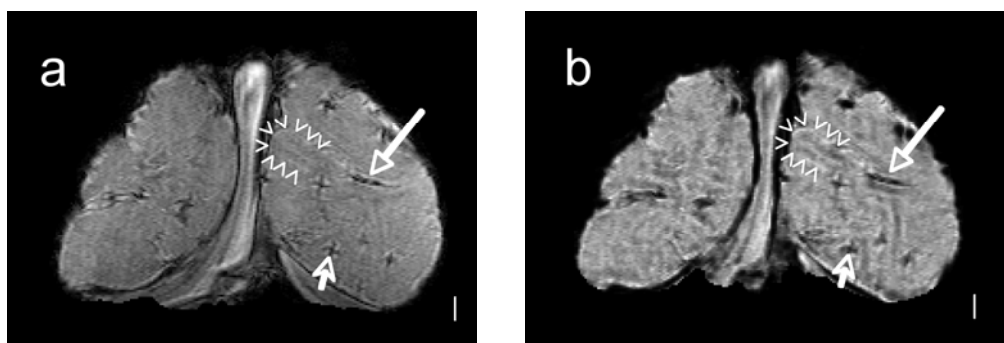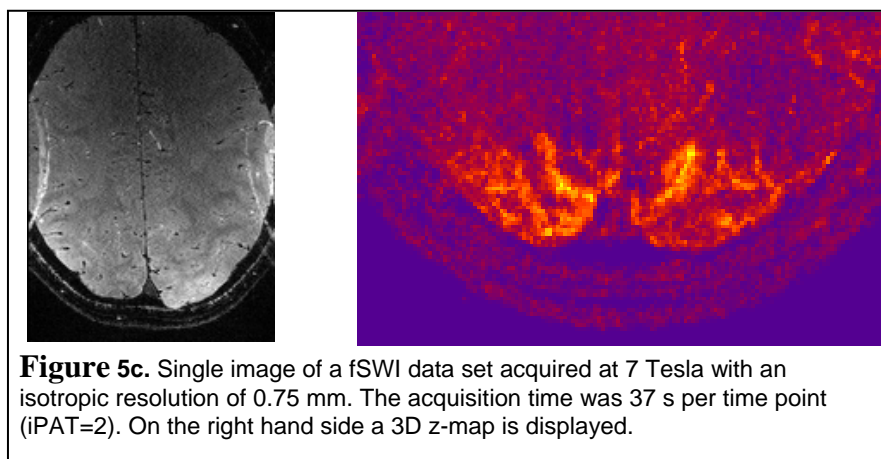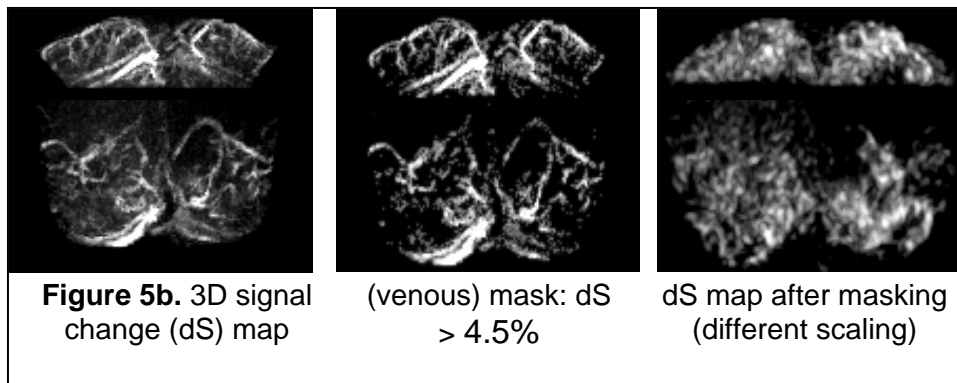
Figure 5b. 3D signal change (dS) map   (venous) mask: dS > 4.5%   dS map after masking (different scaling)

Figure 5c. Single image of a fSWI data set acquired at 7 Tesla with an isotropic resolution of 0.75 mm. The acquisition time was 37 s per time point (iPAT=2). On the right hand side a 3D z-map is displayed.

Figure 6. (a) Slice through the occipital cortex showing the cross-shaped pattern around the cross section of small veins (small arrow; resolution: 0.5 mm isotropic, 3 Tesla). Long arrow points to a vein running in-plane. Arrowheads follow the shape of a sulcus. (b) The processed SWI image.
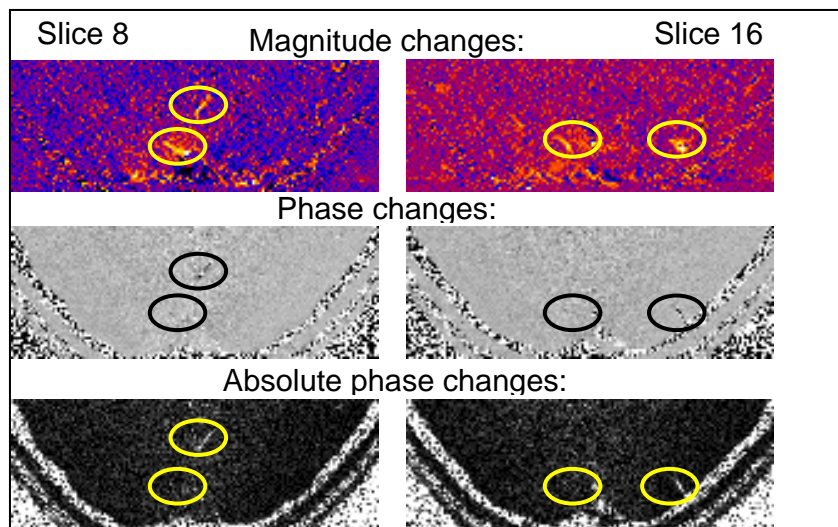

Figure 6c. Phase changes that accompany magnitude changes in fMRI. From top (magnitude changes) over middle (phase changes) to bottom (absolute phase changes – as phase changes can also be negative).
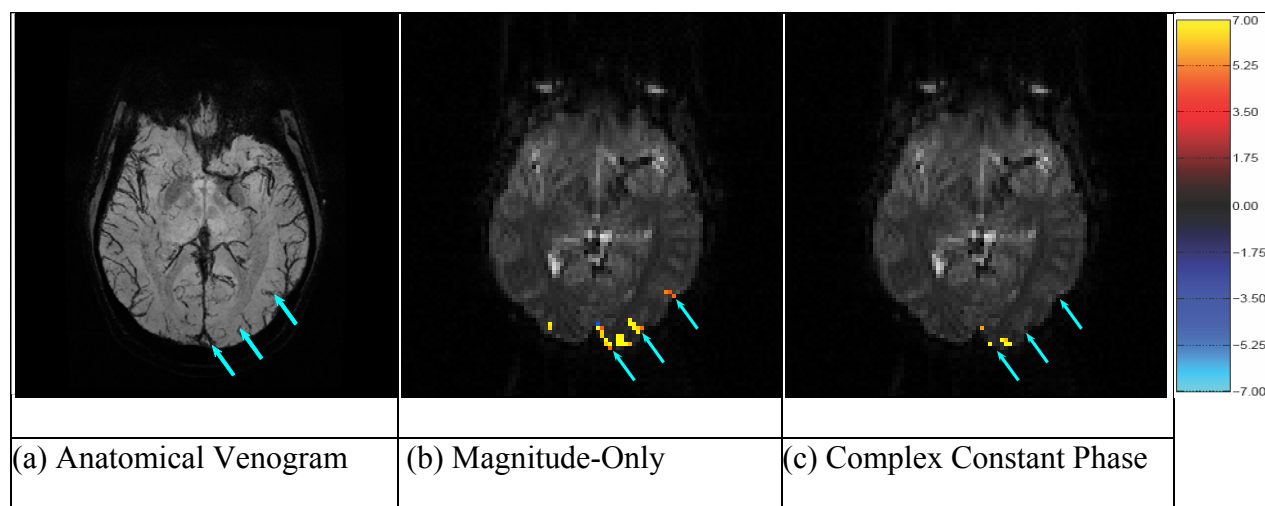
Figure 7. (a) Minimum intensity projection of the venogram through the functional slice and its two neighboring slices. **(b)** Magnitude-only activations from the visual task include regions of activation with a high correspondence to draining veins (arrows). **(c)** Complex constant phase activations exclude the obvious draining vein activations while preserving a cluster of voxels in which no large draining veins are observed.

Figure 8. Complex-valued voxel time series.

(a) Magnitude-Only | (b) Phase-Only | (c) Complex Constant Phase

Figure 9. Simulation z-statistic activation power surfaces. The CP method biases against larger TRPCs. The MO and PO methods are dependent upon only CNR and task-related phase change (TRPC), respectively. The CP method biases against larger TRPCs.